Electronic and nuclear thermal spike effects in sputtering of metals with energetic heavy ions

H. D. Mieskes,* W. Assmann, and F. Grüner
Sektion Physik, Ludwig-Maximilians-Universiät München, D-85748 Garching, Germany

H. Kucal, Z. G. Wang,† M. Toulemonde
Centre Interdisciplinaire de Recherches Ions Laser, BP 5133, 14070 Caen-Cedex 05, France
(Received 28 November 2002; published 29 April 2003)

Sputtering yields and typical angular distributions of pure metals were measured with heavy ions at energies where electronic energy loss dominates. Using different ion charge states and ion/energy combinations, electronic effects were observed in sputtering of metals such as Ti and Zr, but not for Au. An inelastic thermal spike model was extended to calculate sputtering by particle evaporation from an ion track, however, to reproduce the measured yields, besides electronic also elastic collision (nuclear) spike effects had to be included. The results demonstrate the importance and synergism of both heating mechanisms for sputtering in this energy regime.

DOI: 10.1103/PhysRevB.67.155414 PACS number(s): 79.20.Rf, 63.20.Kr, 82.80.Yc

I. INTRODUCTION

Sputtering experiments on insulators with heavy-ion beams at energies where electronic stopping dominates have shown much larger yields[1,2] than what could be explained by linear collision cascade theory.[3] The observed sputtering yields were attributed thereof to electronic effects. The situation was similar to the earlier observation of nuclear tracks in insulators, which could also not be explained by collision cascades. Realizing the close relation of nuclear tracks to surface erosion[4,5] similar scenarios were proposed to describe the way from the initial electronic excitation and ionization of the target atoms to their final ejection. One idea was evaporation by an electronically heated thermal spike process,[6] another one direct ejection due to an ion explosion mechanism,[7] and even a combination of both has been suggested: heating by Coulomb explosion and consecutive evaporation out of a thermal spike.[8] All these models, of course, have been developed to explain electronic effects in insulators, therefore it was a general belief that the proposed mechanisms should be ineffective in conductors and electronic effects insignificant in metals.[9,10] Partly because of this expectation very few attempts have been made to measure sputtering yields of pure metals in the electronic stopping regime, partly also due to experimental difficulties originating from the oxidation problem. Metal oxides are hard to avoid under normal vacuum conditions and, as insulators, they can completely dominate the sputtering yield. Sputtering experiments in the past on pure metallic targets with energetic heavy ions at well-controlled surface conditions were made by O'Connor *et al.*[11,12] Using 70-MeV Br projectiles and Nb targets, no electronic sensitivity could be observed and the measured yields turned out to be compatible with nuclear sputtering.

The situation changed as high-energy heavy-ion beams with electronic stopping power (S_e) well above 10 keV/nm became available for irradiation experiments. Systematic studies of damage creation in conductive materials revealed clear electronic effects such as anisotropic growth phenomena,[13,14] amorphization of crystalline structures,[15] defect creation,[16,17] and even latent tracks were observed in metallic alloys.[18] In the process of stopping fullerene beams through which even higher energy densities can be produced, tracks have been discovered in pure metals as well.[19] However, the huge sputtering yields of Au and Ag targets induced by keV/u Au cluster beams were clearly related to nuclear stopping (S_n).[20,21] Thus, despite the observation of electronic sensitivity above certain energy loss thresholds, to our best knowledge clear electronic sputtering of pure metals has not yet been observed.

Effects of the electronic stopping power in metals have been simulated within the framework of an (inelastic) thermal spike model using thermodynamic concepts.[16,22] In agreement with a large number of experiments a sensitivity to electronic effects was found for metals which have strong electron-phonon coupling and/or a low melting point. Moreover, calculated track radii defined by the molten zone around the ion path and thresholds for damage creation could reproduce the existing measurements or were predicted for other metals where no data existed.[22,23] An experimental test of these predictions could further strengthen the reliability of a thermodynamic concept for electronic spikes. This motivated a systematic study of sputtering yields in our laboratory, assuming a similar connection in metals between track formation and sputtering as for insulators. Sputtered particles, however, leave the surface much earlier than track formation is finished or any annealing mechanism may have already worked. Thus, additional information about electronic effects in solids could be expected from sputtering experiments.

In this paper, we report on systematic sputter measurements with heavy-ion projectiles on two metals, Zr and Ti, for which electronic effects have been predicted within the investigated energy range. Additionally, since Au is expected to be insensitive to electronic effects and is well studied in the nuclear stopping regime, sputtering yields of Au have been measured for comparison. In the first part of this paper we discuss the considerations of target surface-related problems as well as precautions necessary to avoid surface contaminations and surface roughness effects. By using different

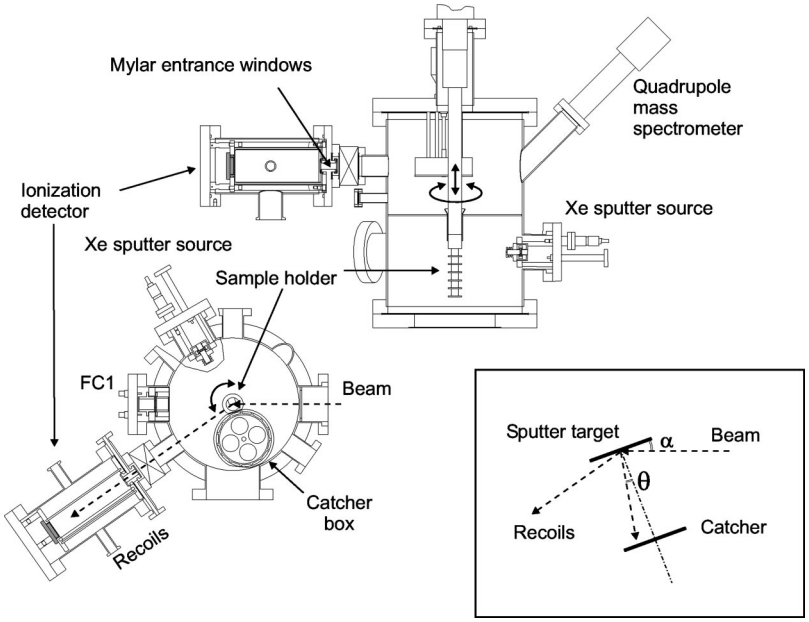

FIG. 1. Schematic of UHV setup and the experimental geometry.

heavy ions at different energies and charge states, clear evidence for electronic effects has been found in the experimental results. This was confirmed in Monte Carlo (MC) simulations of sputtering by elastic collisions which significantly underestimated the measured yields. In the last part of this paper the existing inelastic thermal spike model[16,22] is extended to calculate sputtering yields. The measured yields and energy dependencies, however, can only be reproduced by assuming simultaneous electronic and nuclear heating.

II. EXPERIMENT

A. Experimental setup

When measuring sputtering yields of metals with high-energy heavy ions one is confronted with two very special problems: the low beam current possible and the sensitivity of metals to oxidation. In this study of electronic sputtering effects, metal oxides, being insulators, are extremely dangerous because of their known large sputtering yields at high energies. Since most of the sputtered atoms originate from the first atomic layers, even a monolayer of oxide could falsify the real metal sputtering yield and must be excluded. Sputtering, however, is a surface cleaning process in itself and thus a contamination-free surface can be obtained if the incoming particle flux multiplied by the sputtering yield is larger than the adsorption rate for contaminants. As a rule of thumb, this rate lays around 10^{15} atoms/cm^{-2} s^{-1} at a vacuum of 10^{-6} mbar. In keV sputtering with a typical ion flux of 10^{16} ions/cm^{-2} s^{-1} the self-cleaning condition can easily be fulfilled. For ions in the 100 MeV range, however, the ion flux has to be limited to 10^{12} ions/cm^{-2} s^{-1} in order to exclude target melting and vaporization. This low flux inhibits sufficient sputter cleaning during the irradiation itself and contamination-free surfaces can only be assured through ultrahigh vacuum (UHV) techniques.

Therefore, a special UHV setup has been developed at a beam line of the Munich tandem accelerator laboratory, described in detail elsewhere.[24] The essential parts of the UHV chamber and the irradiation geometry are shown in Fig. 1. By means of two differential cryopumping stages and after the usual bakeout of all internal structures at about 250 °C a basic vacuum of 10^{-10} mbar could be reached in the sputtering chamber with the beam on target. The final vacuum composition was checked by a quadrupole mass spectrometer giving hydrogen as the dominant remaining component. The sputter targets, mounted on a sample holder with five mounting positions, could be moved with a vacuum manipulator in front of a 8 keV Xe sputter source for *in situ* surface cleaning. Thus, contamination-free surfaces could be prepared and maintained for several hours.

As important as cleaning was the monitoring of surface conditions during the experiment. Here we made use of the irradiating beam itself which offered in oblique incidence, besides enhanced sputtering yields, the possibility of elastic recoil detection analysis (ERDA) for surface contamination checks. A ΔE-E_{rest} detector telescope was developed for this purpose whose ΔE detector consisted of a position-sensitive gas ionization chamber whereas the remaining energy was measured with a 20×20-mm^2 p-i-n diode.[24] The compatibility problem of a gas-filled detector in close connection to an UHV setup was solved by a differentially pumped Mylar entrance window of 2.4 μm total thickness which could be backed at moderate temperatures. The detector setup had a solid angle of 1.8 msr mounted at a scattering angle of 35°, and offered the advantage of a low-energy threshold for heavy-ion detection, a radiation-resistant transmission detector, as well as a position sensitivity for kinematic correction to reach good depth resolution despite the large acceptance angle.[25] Hence surface oxygen could be easily distinguished from bulk contamination, and continuous monitoring of oxidation was possible. The irradiation geometry in this work is defined by two angles, the incidence angle α of the incoming ions measured to the sputter target surface, and the exit angle θ of the outgoing sputtered particles measured to the target surface normal (see Fig. 1).

B. Irradiation-induced target structure effects

Sputtering as a surface process is sensitive not only to surface contamination but also to surface structure and morphology. The influence of crystal grain size on sputtering yields has been shown for energetic projectiles.[9,26] Thus representative Ti, Zr, and Au targets were tested for their structure and grain size by X-ray diffraction (XRD) and electron microscopy, respectively, before and after heavy-ion irradiation. All targets had a polycrystalline structure with some texture, and a large grain size on the order of many μm was observed, hence well above the critical size of 10–100 nm for ''grain-size'' effects. This original structure was not changed after irradiation with typical fluences of 10^{13} ions/cm^2.

Irradiation-induced surface roughness formation is known from high-energy irradiation experiments[27] and this could influence the sputtering yield determination. This effect was clearly observed both in experiments and in simulations of sputtering at low energies by distorting the angular distribution which enters in the calculation of the total yield.[28] In order to check for similar effects at high energies we irradiated Au, Zr, and Ti targets with 230 MeV Au ions at different fluences up to 10^{16} ions/cm^2 and measured the surface roughness before and after with atomic force microscopy. The targets evaporated onto Si wafers had originally a mirror-like surface with a mean roughness below 20 nm. The 8 keV Xe sputter cleaning process with varying incidence angle did not produce any significant change in roughness. The surface roughness of Au and Zr targets increased after high-energy irradiations at a typical fluence of 1×10^{15} ions/cm^2 to a mean value of 50 nm, whereas Ti at this fluence exhibited distinct surface structures with 400 nm mean roughness. Twice this fluence increased the roughness of Ti to some μm, and even at 2×10^{14} ions/cm^2 the mean value was above 100 nm. This surface roughness could not be explained by sputtering itself and thus was apparently caused by the high electronic energy deposition. But due to the limited number of targets which could be mounted for a single experiment a compromise had to be made between fluence per beam spot and surface roughness in order to avoid any distortion of the angular distributions.[29]

C. Sputtered particle detection

Most of the known detection techniques for sputtered particles are not sensitive enough at this low beam current and the correspondingly small number of sputtered target atoms. Secondary ions can be measured with great sensitivity but they represent only a small part of the total yield for metals.[30] Therefore the collection of sputtered particles on catchers was thought to be the best choice, which also offered the additional possibility of measuring angular distributions. The catcher technique has the further advantage of collecting all ejected species irrespective of mass, i.e., atoms and clusters as well, and this feature may be of importance in electronic sputtering. Si wafer material was used as catchers due to its high purity. The lighter mass of Si compared to all the envisaged sputtered atoms reduced the backscattering possibility, making the assumption of a sticking coefficient close to 1 more probable. Nevertheless, a very sensitive detection technique was necessary due to the expected submonolayer thickness of catched secondaries. Heavy-ion Rutherford backscattering (RBS) analysis with 1.5 MeV C ion beams has the required sensitivity, especially in channeling conditions, another advantage offered by the monocrystalline Si catchers. Under these conditions 10^{13} Ti atoms/cm^2 and 10^{11} Au atoms/cm^2 could be measured within reasonable time.[24] Fourteen catchers were mounted in a well-shielded magazine where one catcher after another could be rotated in front of an aperture opposite the sputter target to collect sputtered particles from different irradiations. This setup allowed differential yields to be measured at $\theta=0°$ with an angle uncertainty of $\pm2°$ mainly defined by the RBS beam spot. For angular distributions a second box was available with three arcs of nine catchers at a larger distance of 40 mm to the beam spot covering angles θ between $+40°$ and $-40°$. Spot size and mechanical tolerance cause here an angle uncertainty of $\pm5°$. However, the impossibility of reloading new catchers during one experiment due to the UHV conditions limited the number of measured angular distributions in this study.

D. Experimental procedure

The experiments were performed with Au, Zr, and Ti sputter targets produced by electron-beam evaporation of purified material onto Si with thicknesses of 1.5 μm. Targets were sputter cleaned by 8 keV Xe ions *in situ* at different incidence angles right before the experiments. This might have also helped to prepare steady-state conditions which could not be reached during the experiment due to the low ion fluence. According to the ERDA monitor the surface oxide layer was reduced by this sputter cleaning process to at least 0.01 ML, i.e., 10^{13} O atoms/cm^2, and did not significantly change during 3 h of irradiation at 10^{-10} mbar.[24] As expected the surface contamination of Au targets was below 10^{-3} ML even at a vacuum pressure of 10^{-7} mbar.

I and Au ions were delivered from the Munich 15 MV tandem accelerator with energies ranging from 55 to 275 MeV to get a wide variety of energy-loss values. The charge state dependence of the sputtering yield was tested for each energy by measuring, first, with an ion charge state delivered by the terminal stripper and defined by the analyzing magnet, and second, after a carbon stripper foil in front of the sputter target. The mean charge state after this post-stripper was typically about two times higher than the incoming charge state, e.g. for 230 MeV Au ions there was an increase from $16+$ to $\langle 29+\rangle$. The incident particle flux was measured with the ERDA detector in two independent ways: by the total count rate calibrated by a Faraday cup with a suppression electrode in front (FC1, see Fig. 1) and by measuring the number of target recoils. Both methods came within 10% to the same result. The Faraday cup was also used to determine the average ion charge state of the projectiles after inserting the additional stripper foil in front of the sputter target assuming a symmetric charge state distribution.

The typical spot size of the ion beam at the incidence angle $\alpha=18°$ was 3×3 mm^2 on targets of 12×12 mm^2

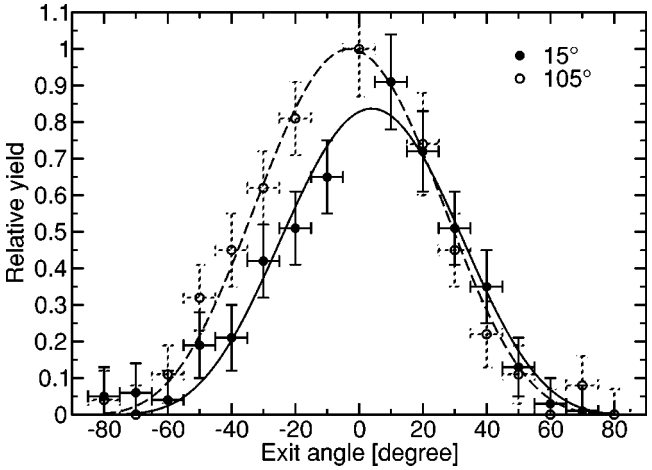

FIG. 2. Angular distribution of Au particles sputtered with 210 MeV I^{15+} ions. The catcher arc was tilted by 15° and 105° to a plane perpendicular to the incoming ions.

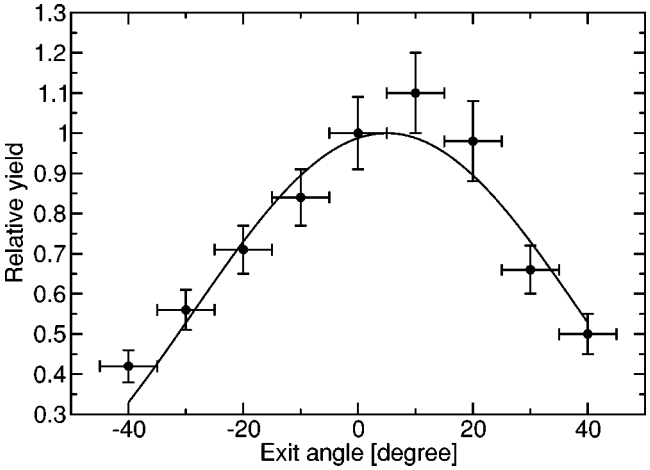

FIG. 3. Angular distribution of Zr particles sputtered with 230 MeV Au^{16+} ions.

size. The beam spot was adjusted by means of an CsI crystal on the sample holder and an outside video camera. All irradiations were performed at room temperature with a typical particle current of some pnA (10^{11} ions/cm^{-2} s^{-1}) and thus target heating was negligible. As discussed later the fluence per beam spot had to be limited to some 10^{14} ions/cm^2 to avoid excessive surface roughening, therefore, a total fluence of 10^{15} ions/cm^2 was collected for each target by moving the sputter target to different irradiation spots.

III. EXPERIMENTAL RESULTS

A. Angular distributions and incidence angle dependency

Due to the differential sputtering yield measurements limited to $\theta = 0°$ in most cases the total yields had to be calculated assuming a certain angular distribution. The corresponding angular distributions of sputtered particles are, however, unknown at these energies. Therefore exemplary angular distributions were measured for all targets at UHV conditions including a study of surface roughness effects. The angular range of our UHV arc catcher setup was restricted to $-40° < \theta < +40°$. However, for Au targets where less surface contamination could be expected additional measurements were made with a full angle range in our ERDA setup[25] at a vacuum pressure of 10^{-7} mbar. Here we used a double arc geometry with ultrapure Al catcher foils covering $-90° < \theta < +90°$. One arc plane had an angle of 15° to the incident beam, the other one of 105°. This configuration could also test for azimuthal symmetry around the surface normal. The catcher surface was in all these measurements perpendicular to the incidence direction of the sputtered atoms to assure equal sticking probability at all angles.

Angular distributions for Au and Zr targets are shown in Fig. 2 and Fig. 3 with 210 MeV I^{15+} and 230 MeV Au^{16+} ions, respectively. The experiment in double arc geometry indicates an azimuthal symmetry within the experimental errors. The distributions can be fitted by a cosine function $\cos^x\theta$ with $x = 4.0$ and 4.3, respectively. A compilation of all the angular distribution experiments is given in Table I showing the general trend for exponents to be around 3. This overcosine behavior was observed by other groups in sputtering experiments at MeV energies, too.[11,31] However, from Monte Carlo simulations with TRIM-CASCADE (TC) (Ref. 32) generally lower exponents of about 1.5 are deduced (Table I). These exponents are similar to those extracted from keV sputtering experiments as well as from simulations.[33,34] It should be mentioned that no effect of texturing was seen in the angular distribution of the polycrystalline targets with either ⟨100⟩ or ⟨110⟩ preferential orientation.

The influence of surface roughness on the angular distribution can be clearly seen in Fig. 4. Here the angular distribution of an initially polished Ti target is shown after a fluence of about 3×10^{15} ions/cm^2. The measured mean roughness of a few μm caused a distinct shift of the yield maximum, opposite to the beam incidence direction. At 10 times less fluence a mean roughness of about 120 nm was measured with an almost symmetric angular distribution around the surface normal. In order to understand this effect and correlate it with surface roughness a simulation program was developed, which probed a certain surface topology with parallel projectile trajectories.[29] One problem in these calculations was to model the rather complicated surface structure,

TABLE I. Angular distribution parameters of sputtered particles from different targets. Projectiles were indenting at $\alpha = 18°$; ions with their charge state and energy are indicated. The exponent x of the fit function $\cos^x\theta$ is given as determined from the experiment and from TC simulation.

Ion	Energy (MeV)	Target	Fluence ions/cm^2	$\cos^x\theta$ x_{exp}	x_{TC}
I^{15+}	210	Au	6.65×10^{14}	4.3 ± 0.4	1.76
				4.0 ± 0.3	
Au^{16+}	230	Au	1.13×10^{15}	3.6 ± 0.2	1.75
			4.51×10^{14}	3.3 ± 0.3	
		Ti	3.75×10^{14}	2.5 ± 0.5	1.42
		Zr	1.23×10^{15}	3.2 ± 0.4	1.44

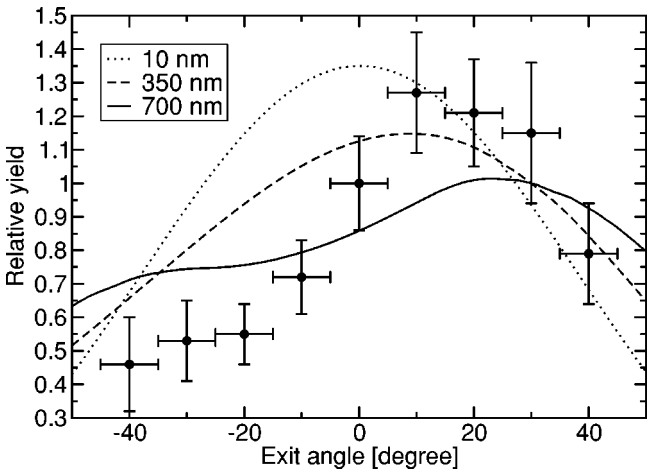

FIG. 4. Angular distribution of Ti particles sputtered with 230 MeV Au^{16+} ions form a surface with a few μm mean roughness. The result is compared to a simulation where different surface roughnesses are assumed.

as seen in electron microscopy, and its change during the irradiation. The result of such simulations for different roughnesses is compared in Fig. 4 with the measured distribution. The characteristic shift and slope of the distribution is well reproduced, but in view of the necessary simplification of the topology the simulation can only give an estimate of the effect. Nevertheless, to avoid too large a roughness influence we used a fluence limit during irradiations of Ti on individual target spots of 5×10^{14} ions/cm^2. This beam-induced roughness problem was found to be less severe for Zr and Au targets.

The incidence angle dependence of the sputtering yield enters in comparisons between measurements and simulations as well. No data were available on this dependency at high energies and especially on its roughness dependence. For the latter we trusted our simulation[29] which reproduced low-energy sputtering data of Küstner *et al.*[28] and did not show any influence of the surface roughness on the incidence angle. The incidence angle could be varied in our ERDA setup from vertical to flat incidence, thus exemplary measurements were performed on smooth Au targets at incidence angles α of 90°, 55°, and 20° with 230 MeV Au ions. An increase of the yield was measured from $\alpha=90°$ to $\alpha=20°$ by a factor of 5.0, slightly steeper than 3.8 as calculated by TC for pure nuclear sputtering. The measured incidence angle dependence could be fitted by $\sin^{-f}\alpha$ with a best-fit value of $f=1.5$.

B. Charge state and energy loss dependence

In order to discriminate between nuclear and electronic effects in sputtering we used ion/energy combinations where the nuclear energy loss S_n was similar for a certain target material and the electronic loss S_e different, and vice versa. Thus the electronic energy loss varied from 11 keV/nm to 60 keV/nm and the nuclear from 0.1 keV/nm to 1.1 keV/nm. All our experimental results on Ti, Zr, and Au targets are summarized in Tables II–IV. Note that all yields are given for the experimental incidence angle $\alpha=18°$. The results are presented separately for projectiles with a single charge state if defined by the analyzing magnet after the accelerator, and for those around the mean charge state if produced by post-stripping. The projectile energy loss at the target surface in Tables II–IV was calculated with SRIM96,[35] which takes into account the velocity-dependent equilibrium charge state.

The experimental differential yield $Y_{diff}(0,R)$ was measured at 0° and at a distance R. The total yield Y_{exp} was

TABLE II. Total sputtering yield of Ti for different ions, charge states, and energies at an incidence angle $\alpha=18°$ to the target surface. $\langle\ \rangle$ indicates a charge distribution with mean charge state. S_e and S_n denotes electronic and nuclear energy losses according to SRIM96. Y_{exp} is integrated from the measured differential yield at 0 ° assuming a $\cos^{2.6}$ angular distribution for all energies, given without systematic errors (see text). Y_{TC} is calculated by TC for an 18° incidence angle and Y_{TS} by a thermal spike (TS) model with $g=1.0\times10^{13}$ W/cm^3 K, corrected by $\sin^{-1.5}$ for the incidence angle; Y_{TC+TS} is the sum of both, and R_0 denotes the calculated spike radius.

Ion	Energy (MeV)	S_e (keV/nm)	S_n	Y_{exp}	Y_{TC} (atom/ion)	Y_{TS}	Y_{TC+TS}	R_0 (Å)
$Au^{\langle 29+\rangle}$	275	30.3	0.18	6.5±1.0	0.8	4.1	4.9	7.0
Au^{18+}	275	(15) [a]	0.18	3.5±0.5	0.8	0.5	1.2	7.0
$Au^{\langle 29+\rangle}$	230	29.0	0.21	7.4±1.1	0.9	4.1	5.0	7.5
Au^{16+}	230			3.7±0.6				
$Au^{\langle 26+\rangle}$	109	22.3	0.37	8.9±1.3	1.6	3.7	5.3	9.5
Au^{11+}	109			5.8±0.9				
$I^{\langle 29+\rangle}$	210	22.6	0.07	2.8±0.3	0.3	0.8	1.1	5.0
I^{15+}	215			1.2±0.2				
$I^{\langle 21+\rangle}$	55	14.1	0.22	2.5±0.3	1.0	0.7	1.7	8.0
I^{7+}	55	(7) [a]	0.22	2.2±0.3	1.0	0.4	1.4	8.0

[a]Assumed S_e value of nonequilibrium charge state for TS calculation.

TABLE III. Total sputtering yield of Zr for different ions, charge states, and energies at an incidence angle $\alpha=18°$ to the target surface. Assumed angular distribution for Y_{exp} total yield integration was $\cos^{3.2}$; for TS calculations $g=2.6\times10^{12}$ W/cm^3 K was used. For further explanation see Table II.

Ion	Energy (MeV)	S_e (keV/nm)	S_n	Y_{exp}	Y_{TC} (atom/ion)	Y_{TS}	Y_{TC+TS}	R_0 (Å)
$Au^{\langle 29+\rangle}$	275	32.3	0.23	2.9±0.3	1.0	1.4	2.4	8.0
Au^{18+}	275	(16) [a]	0.23	1.9±0.2	1.0	0.2	1.2	8.0
$Au^{\langle 29+\rangle}$	230	30.3	0.27	2.9±0.4	1.1	1.4	2.5	9.0
Au^{16+}	230			1.7±0.2				
$Au^{\langle 26+\rangle}$	109	21.8	0.47	5.5±0.7	1.9	1.8	3.7	11.0
Au^{11+}	109			3.6±0.4				
$I^{\langle 28+\rangle}$	210	24.4	0.10	0.8±0.1	0.5	0.2	0.7	6.0
I^{15+}	210	(12) [a]	0.10	0.5±0.1	0.5	0.01	0.5	6.0
$I^{\langle 20+\rangle}$	59	14.8	0.26	1.7±0.2	1.4	0.4	1.8	8.0
I^{8+}	59	(7) [a]	0.26	1.3±0.2	1.4	0.1	1.5	8.0

[a]Assumed S_e value of nonequilibrium charge state for TS calculation.

TABLE IV. Total sputtering yield of Au for different ions, charge states, and energies at an incidence angle $\alpha = 18°$ to the target surface. Assumed angular distribution for Y_{exp} total yield integration was $\cos^{3.8}$; for TS calculations $g = 2.3 \times 10^{10}$ W/cm^3 K was used. For further explanation see Table II.

Ion	Energy (MeV)	S_e (keV/nm)	S_n	Y_{exp}	Y_{TC} (atom/ion)	Y_{TS}	Y_{TC+TS}	R_0 (Å)
$Au^{\langle 29+\rangle}$	275	59.8	0.54	12.1±1.5[a]	2.5	3.1	5.6	6.0
Au^{18+}	275	(30) [b]	0.54	12.4±1.4[a]	2.5	2.8	5.3	6.0
$Au^{\langle 29+\rangle}$	230	55.4	0.62	11.8±1.4	3.0	4.1	7.1	6.5
Au^{16+}	230	(30) [b]	0.62	10.6±1.1	3.0	3.8	6.8	6.5
Au^{11+}	109	(36) [b]	1.10	13.4±1.6	5.3	17.2	22.5	8.5
Au^{11+}	109	(36) [b]	1.10	13.4±1.6	5.3	13.1[c]	18.4[c]	8.5
Au^{11+}	109	(17) [b]	1.10	13.4±1.6	5.3	14.3	19.6	8.5
I^{15+}	210	(45.9) [b]	0.22	2.9±0.3	1.1	0.3	1.4	4.5
$I^{\langle 21+\rangle}$	55	22.7	0.63	8.3±1.1	4.1	3.5	7.6	7.0
I^{7+}	55	(11) [b]	0.63	10.3±1.3	4.1	3.1	7.2	7.0

[a]Enhanced yield due to small grain size.
[b]Assumed S_e value of nonequilibrium charge state for TS calculation.
[c]$g = 0$ for TS calculation.

calculated assuming a cosine function $\cos^x\theta$ as determined from the measured angular distributions. The total yield integral can then be written as

$$Y_{exp} = Y_{diff}(0,R)2\pi R^2 \int_0^{\pi/2} \cos^x(\theta)\sin(\theta)d\theta$$
$$= Y_{diff}(0,R)2\pi R^2 (x+1)^{-1} \quad (1)$$

and Y_{exp} calculated with the tacit assumption that x is independent of the energy for one specific ion in this energy range.

Most of the measurements for Au targets were repeated in different experimental runs and reproduced within 15%. Some data points were repeated for Ti and Zr targets as well and a reproducibility was found of about 20% for differential sputtering yields including the error of RBS catcher analysis. Thus we estimate the differential yield error to be 20%. For the experimental error of the total yield we have to consider the uncertainty of the angular distributions (see Table I) which contributes a rather systematic error of about 25% to the total error. In Tables II–IV the total yield error is given without this systematic part since this error does not enter into relative comparisons within one table.

Inspection of Tables II–IV reveals two clear signatures for electronic effects. First, comparing measurements with Au ions of the same energy but different charge states, an increase is seen in Ti and Zr for the higher charge state clearly outside the experimental errors. An almost doubling of the charge state by post-stripping produces without exception at least 50% more sputtering yield. This cannot be explained within the framework of (nuclear) collision cascade sputtering. A dependence of Y_{exp} on the charge state of the incident ion, however, is well known from (electronic) sputtering of insulating materials.[36] Electronic sputtering is related to the electronic energy deposition which in turn depends on the ion charge state as demonstrated in energy loss measurements with different incidence charge states.[37,38] Thus the observed charge state effect is a clear indication of electronic effects in sputtering of Ti and Zr. In contrast, no charge state effect is seen in sputtering of Au targets. For a more quantitative discussion of the charge state dependence an exact knowledge of the energy loss ''history'' of the ions along their path into the material would be necessary, from which the integrated energy deposition near the surface could be calculated. This interesting but complex problem is beyond the scope of this paper as well as is the exact dependence on single charge states. The following quantitative comparisons are restricted, thereof, to the sputtering yields with ions post-stripped to the equilibrium charge state distribution.

We notice a second signature for electronic effects by comparing experiments with similar nuclear (S_n) but different electronic (S_e) energy loss, where nuclear sputtering alone would produce similar yields. Such a case represents sputtering with 55 or 59 MeV I ions and 230 MeV Au ions which have in each material almost the same S_n at the surface but two times more S_e with the heavier projectile. Tables II and III show that the measured yields (Y_{exp}) are higher for Ti and Zr by more than a factor of 2 and follow the S_e increase. The Au yields in contrast (Table IV) are similar within experimental errors, indicating once more the low electronic sensitivity of Au.

However, the S_n influence on sputtering cannot be neglected even in this high-energy regime. An example is the sputtering with 109 MeV Au ions and 210 MeV I ions, where S_e is similar, but S_n differs by more than a factor of 4. As expected for nuclear sputtering, an increase is seen for all targets by about the same factor going from I to Au ions. It should be noticed that the S_n values are almost two orders of magnitude smaller than the corresponding S_e values.

To summarize, the experiments have revealed angular distributions which are more peaked around the surface normal than at keV energies. Clear evidence has been found for electronic effects for Ti and Zr in the charge state and energy-

loss dependence, but the effects are by far not as large as for insulators and thus nuclear contributions are still apparent.

IV. THEORETICAL CALCULATIONS

A. Comparison to MC simulations

Sputtering caused by collisional cascades (nuclear sputtering) can be simulated by programs such as TRIM-CASCADE (TC),[32] SRIM96,[35] or TRIM-SP.[39] These programs use the TRIM algorithms for calculating the electronic and nuclear stopping powers, and tabulated values for the surface binding energy. The total yield integration of particles surpassing this energy is performed with internally calculated angular distributions. Measured sputtering yields in the nuclear stopping power regime are typically reproduced within a factor of 2, but it should be mentioned that different programs vary by the same factor. The measured yields (Y_{exp}) are compared in Tables II –IV with MC simulations by TC (Y_{TC}). The calculated yields reproduce qualitatively the trend for different energies and ions, but most of the experimental values are underestimated in the case of TC, typically by about a factor of 3 for Au and Zr and up to a factor of 8 for Ti, which is clearly outside experimental errors and TC uncertainties as well. This points clearly to non-cascade contributions in the observed yields. The calculated TC values must follow the nuclear energy loss, and Y_{TC} shows, for example, a small decrease going from 55 or 59 MeV I ions to 230 MeV Au ions in Ti and Zr. This is in strong contrast to the measured distinct increase and is again a hint for non-cascade contributions.

B. The inelastic thermal spike (TS) model

Only a small fraction of the energy of the incident heavy ions is indeed stored in collision cascades at these energies and the major part is distributed in the electronic subsystem of the target by electronic excitation and ionization. The (inelastic) thermal spike[16,22] model was developed to describe the energy transfer from the electronic to the atomic system via electron-phonon coupling. This is assumed to be the dominant energy transfer mechanism, because a Coulomb explosion of the ionized atoms is not effective in conductors due to the experimentally shown large mobility of the electrons.[40] The inelastic TS model considers the electrons in a metal to be described by a quasi-free-electron gas and the thermodynamic properties of the atomic lattice by experimentally known parameters. The time scale of a thermal spike is very short since the energy is deposited by the heavy-ion projectiles within 10^{-16} s, shared between the electrons within 10^{-15} s, and thermalization in the lattice occurs within 10^{-13} s, thus the use of equilibrium thermodynamic parameters may be questionable. However, this approach has reproduced a large number of effects in the electronic stopping power regime and is the only quantitative model at present.

Following the description in Refs. 16 and 22 the energy diffusion in the electronic and atomic subsystems at time t and at a distance r from the ion track assuming cylindrical geometry is described by two coupled differential equations,

$$C_e(T_e)\frac{\partial T_e}{\partial t}=\frac{1}{r}\frac{\partial}{\partial r}\left[rK_e(T_e)\frac{\partial T_e}{\partial r}\right]-g\cdot(T_e-T_l)+A(r,t), \tag{2}$$

$$C_l(T_l)\frac{\partial T_l}{\partial t}=\frac{1}{r}\frac{\partial}{\partial r}\left[rK_l(T_l)\frac{\partial T_l}{\partial r}\right]+g\cdot(T_e-T_l), \tag{3}$$

where $T_{e,l}$, $C_{e,l}$, and $K_{e,l}$ are the temperature, specific heat, and thermal conductivity for the electronic system and the lattice, respectively. The initial energy density $A(r,t)$ is taken from a spatial distribution function $F(r)$ of the delta-ray energy deposition[41] and a Gaussian distribution in time $G(t)$:

$$A(r,t)=bS_e\cdot G(t)F(r)=bS_e\cdot\exp[-(t-t_0)^2/2t_0^2]\cdot F(r), \tag{4}$$

with t_0 equal to 10^{-15} s is the time required for the electrons to reach thermal equilibrium. At $4t_0$ the energy deposition is stopped in the calculation. b is a normalization constant so that the total energy input is equal to S_e.

Depending on the amount of energy transfered to the atomic system and the reached temperature, specific phase changes can be induced such as transitions from the solid to liquid phase or liquid to vapor phase. A fast quench of these phase changes is supposed to freeze the defect, and this has been experimentally observed.[16,42,43] The only free parameter in the calculations is the electron-phonon coupling value g which has been determined by fitting electronic stopping power thresholds for damage creation in several metals, assuming that they are formed during the quench of a molten phase. The electron-phonon coupling value g can be calculated as follows using parameters of the specific material:[22]

$$g=\frac{\pi^4(k_B z n_l v_s)^2}{18K_e(T_e)}, \tag{5}$$

where v_s is the sound velocity, n_l the atomic density, and z the number of electrons participating in the thermal spike. Calculated values for noble metals with $z=1$ are quite in agreement with those determined by fs laser experiments[44] or from thermal-conductivity measurements.[16,45] The two parameters in Eq. (5) on which g mainly depends are the thermal conductivity and the sound velocity. The latter is proportional to the square of the Debye temperature,[22] which by itself is inversely proportional to the atomic mass of the materials. Furthermore the thermal conductivity of Au is at least one order of magnitude larger than the one of Zr or Ti. Both dependencies together result in a two orders of magnitude difference of the g values of Au and Zr or Ti, respectively, which is also seen in fs laser experiments.[44] This difference mirrors the individual density of electronic states at the Fermi energy, too, and explains the different electronic behavior of these metals.

Very different effects could be reproduced by this inelastic TS model: the influence of the irradiation temperature,[46] the velocity effect,[43,47-49] electronic annealing in Fe,[43,49] and even track diameters of C_{60} cluster beams.[50] This supports the reliability of the TS model and the thermodynamic concept behind it.

C. Extension of the inelastic thermal spike model to sputtering

The existing TS model, however, was not developed to calculate sputtering yields that may be regarded as a logical extension of the model. Indeed sputtering could be linked to the evaporation of particles at the surface of the irradiated material and consequently damage creation (melt phase) and sputtering (vapor phase) should be described with the same set of parameters. Thus the TS model was extended to calculate the number of evaporated atoms for the metallic targets in this study. Similar to Sigmund and Claussen's approach for sputtering by elastic-collision spikes[51] a statistical thermodynamic ansatz was made using a Maxwell-Boltzmann equation to describe the thermal distribution of the target atoms. Following this concept the evaporation rate ϕ can be written as

$$\phi[T_l(r,t)] = N_{at}\sqrt{k_B T_l(r,t)/(2\pi M)} \cdot \exp[-U_s/k_B T_l(r,t)], \tag{6}$$

where $k_B T_l(r,t)$ is the energy of a lattice atom with mass M at a radial distance r and at a time t. N_{at} is the number of atoms per cm^3 and U_s is the surface binding energy which is usually equated with the sublimation energy. For the thermal conductivity of those atoms above vaporization temperature we used values derived by Sigmund[52] which increase with the square root of the temperature. By integration of Eq. (6) over time t and space r, one can deduce the total sputtering yield Y_{TS}. Instead of Sigmund and Claussen's analytical solution, these equations were used inside the existing TS program which calculates numerically the energy and temperature development in time and space. In order to compare it with the experimental results the calculated values were corrected for the measured incidence angle dependence by $\sin^{-1.5}\alpha$.

No free parameter exists in the extended TS sputtering calculations if we want to be consistent with earlier TS calculations of electronic effects in metals.[22] From fits of electronic damage thresholds and various track radii in Ti,[19,42] an electron-phonon coupling value $g = 1.0\times10^{13}$ W/cm^{-3} K^{-1} was deduced. TS computation results with this value are compared in Fig. 5 to the experimental results of Ti where the collision cascade contribution calculated by TC was added for better comparison. The TS simulation is in the same range as the experiments, but the general trend with the energy is not reproduced, and the yields are obviously underestimated by a factor of 2–3.

Due to the fast time scale for the energy transport in the lattice of less than 10^{-13} s typically superheating can occur. In this situation the matter can reach higher temperatures leading to faster cooling rates. Superheating has been demonstrated in pulsed laser irradiations with fs pulse lengths.[53,54] In the above calculation this scenario of superheating has been simulated by ignoring the latent heat. Calculations with latent heat for the Ti case have revealed sputtering yields more than one order of magnitude higher than the measured ones. Thus we decided to perform all the calculations without latent heat assuming superheating.

However, sputtering yield calculations for Zr using a g value of 2.6×10^{12} W/cm^{-3} K^{-1} as determined by damage creation in Zr at high energies[19,42] failed completely, with or without superheating. Probably due to less effective electron-phonon coupling and the rather high sublimation energy none of the ion/energy combinations delivered an electronic contribution to sputtering. But the experiments have clearly indicated electronic effects in Zr sputtering.

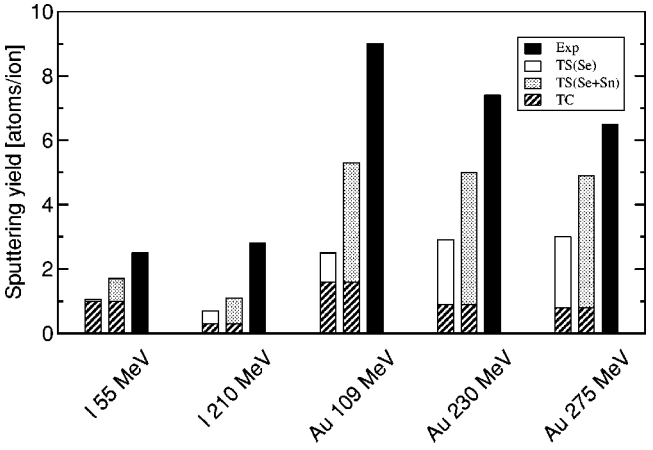

FIG. 5. Simulation of Ti sputtering yields for different ion/energy combinations. Measured values (Exp) are compared to TC simulations (TC) and TS calculations with heating by the electronic energy loss with only Se or together with the nuclear energy loss (Se+Sn).

D. Inclusion of nuclear heating in the inelastic thermal spike model

Since the experimental results also suggested the importance of nuclear energy loss, the energy stored in the collision cascade was taken into account for track heating ("collision spike," see Ref. 30, and references therein) and additionally implemented into our extended TS model. The nuclear energy deposition was added in the equation describing the temperature distribution in time and space of the atomic system [Eq. (3)]. In analogy to the electronic energy density $A(r,t)$ the nuclear energy density $B(r,t)$ is written as

$$B(r,t) = b_n S_n G_n(t) F_n(r), \tag{7}$$

which is normalized to S_n by b_n. The time-dependent part $G_n(t)$ of the energy deposition is approximated by

$$G_n(t) = \exp(-t/\tau), \tag{8}$$

and the exponential decay has a time constant τ which can be estimated from the average energy and respective range of a cascade. According to TRIM-SP simulations a few keV are deposited to each atom, resulting in a typical range of 10 Å. This gives between 10^{-13} s and 10^{-14} s for the deposition time τ as a first approach in agreement with Sigmund.[52] The space distribution $F_n(r)$ of the energy density is written as

$$F_n(r) = 1/r \cdot \exp(-r/R_0) \tag{9}$$

with a "spike radius" R_0 (where 66% of the total nuclear energy is deposited). This quantity is connected to the mean energy and the related mean range of scattered recoils form-

TABLE V. Total sputtering yield of Au on Au at vertical incidence. Y_{exp} is from Ref. 21, TS calculations are with $g=2.3\times10^{10}$ W/cm^3 K, and spike radius R_0 is deduced as in Ref. 20. See also Table II.

Energy (keV)	S_e (keV/nm)	S_n	Y_{exp}	Y_{TC} (atom/ion)	Y_{TS}	Y_{TC+TS}	$Y_{TS(g=0)}$	R_0 (Å)
100	0.8	7.8	54±5	17	60	77	129	22
200	0.9	8.8	62±6.5	19	67	86		23
700	1.8	10.0	79±7	22	84	106	221	24
1400	2.4	9.6	66±5.5	21	76	97		25
3000	3.2	8.2	44±3.5	18	48	66	113	27

ing the collision cascade. Sigmund and Claussen, for example, found a value of $R_0=15$ Å to reproduce sputtering data of Sb on Ag at keV energies.[51] At our much higher energies the mean energy transfer $\langle T\rangle$ to a target atom can be calculated from elastic scattering.[55] In case of Au-Au sputtering, $\langle T\rangle$ varies from 9 keV for 10 MeV incident energy to 230 eV for 300 MeV. Assuming that low-energy atoms are mainly emitted perpendicular to the ion trajectory, one gets spike radii R_0 from 27 Å to 6 Å.

E. TS calculation for Au, Zr, and Ti sputtering

To test the implementation of nuclear heating in the new inelastic TS model, Au self-sputtering was calculated around the nuclear stopping maximum, i.e., for Au ions around 1 MeV, and compared to recent measurements by Andersen *et al.*[20,21] Using a variable R_0 value as deduced from the experimental data and a deposition time $\tau=2\times10^{-13}$ s, the measured yields could be reproduced within a factor of 1.5 (Table V). Y_{TS+TC} includes the contribution from elastic collisions calculated by TC, which by itself represents 40% of the total yield at the most. We have tested the sensitivity of the calculations on the two parameters which were newly introduced into the TS model by the nuclear spike component. The influence of the deposition time τ on the total yield was found to be weak, and a variation from 5×10^{-14} s to 2×10^{-13} s induced only a 10% decrease of the sputtering yield. A change of the spike radius R_0, however, was more important. Using the fixed R_0 value from Sigmund and Claussen[51] of 15 Å increased the TS yield by almost a factor of 2. Although the electronic energy loss and the related energy input are negligible at these energies, the electron–phonon coupling still plays an important role. Reducing the value of g from 2.3×10^{10} W/cm^{-3} K^{-1} to zero increased the calculated yield by a factor of 2–3 demonstrating a cooling effect of the electrons in our TS model.

Introducing the nuclear spike component also in the simulation of our high-energy Au sputtering experiments, where the highest S_n values (1.1 keV/nm) are reached, clearly demonstrates the importance of nuclear heating. Whereas the electronic energy loss alone is not sufficient to evaporate Au atoms (in spite of values up to 60 keV/nm), together with nuclear heating the TS simulation produces a substantial contribution to the sputtering yield. Therewith the total simulated yield (TC and TS added) is in reasonable agreement with the experimental results (see Table IV). A simulation with $g=0$ as shown in Table IV for 109 MeV Au ions lowers the number of evaporated atoms by 25%, pointing to the contribution from the electronic energy loss.

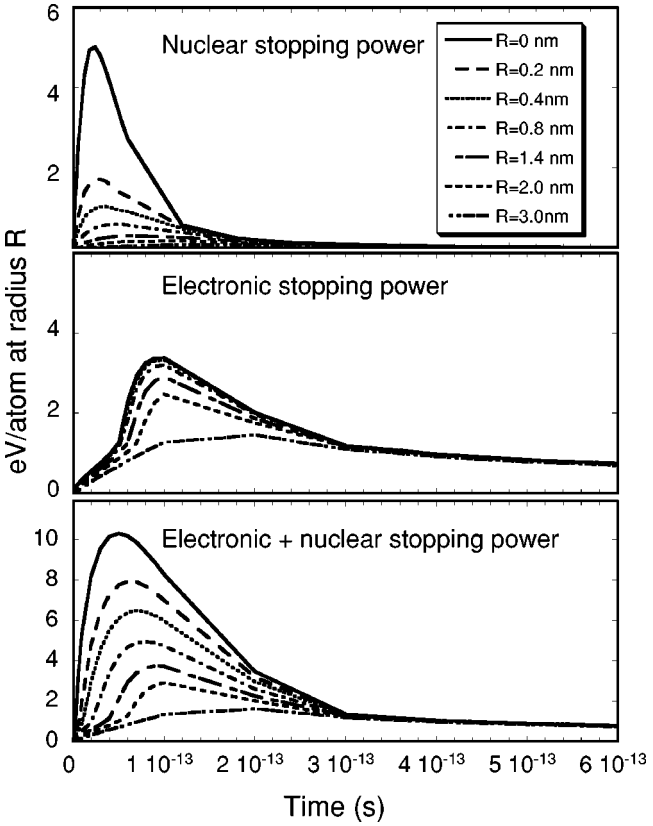

FIG. 6. Simulation with an extended TS model for Zr sputtering. The transfered energy per atom is shown as a function of time for various distances R to the ion path (in this example 230-MeV Au ions with equilibrium charge state). The sublimation energy of Zr is 6.3 eV. The contributions of the nuclear and electronic stopping power are separated.

Repeating the TS calculation for Zr, but now with inclusion of the nuclear component, the synergism of both components becomes obvious. For the case of 230 MeV Au ions with an equilibrium charge state 29+ the calculated time-dependent energy per atom is shown as an example in Fig. 6 at different distances from the ion track. Like electronic heating, as mentioned before nuclear heating alone cannot lift lattice atoms above the sublimation threshold U_s of 6.3 eV. However, with electronic and nuclear heating together, atoms close to the spike center clearly reach energies well above the sublimation energy. From this figure one can also estimate the efficiency with which the nuclear and electronic energy input is transferred to the lattice atoms. A collision cascade created by 0.27 keV/nm nuclear energy loss produces a similar energy per atom as a one hundred times higher electronic energy loss (30.3 keV/nm). This is due to the much more effective elastic-scattering energy transfer compared to the electron-phonon coupling mechanism. All TS calculations for Zr with inclusion of the nuclear energy component are presented in Table III showing remarkably

good agreement with the experimental data. Both the absolute yields and the energy trends are well reproduced.

The addition of a nuclear component improved also the TS result for Ti substantially (see Fig. 5 and Table II). Not only are the absolute yields closer to the experimental results, but also the energy dependence is much better reproduced. The importance of the nuclear contribution becomes evident especially for the lowest Au and I ion energies, where S_n has its largest and S_e its lowest values within this study.

The experimentally observed charge state effect on the sputtering yield was simulated in our TS model using different S_e values. From specific energy loss measurements[37,38] a linear dependence of S_e on different charge states can be deduced as a first approximation. Regarding the factor of almost 2 between the experimentally used charge states, some yield calculations were performed for ion irradiations in a nonequilibrium charge state with half of the SRIM96 energy loss value (given in brackets in Tables II–IV). For Ti and Zr a decrease in the sputtering yield for the lower charge state can be seen whereas for Au the change in S_e does not affect the yield. Thus the electronic sensitivity or insensitivity, seen in the charge state dependence, can be reproduced by the TS model as well.

F. Discussion of the extended thermal spike model

The overall agreement observed between the thermal spike predictions and the experimental results should not hide the hypotheses and assumptions made for the calculations. Electronic sputtering is assumed to be the evaporation of atoms from a hot surface area heated by an inelastic thermal spike. The surface temperature is equated to the bulk temperature as calculated in the TS model in cylindrical symmetry without consideration of any axial gradient. The symmetry break at the surface can certainly influence the surface temperature and could be implemented by an additional coordinate.

The free parameter is the electron-phonon coupling value g for which we have used a value determined by fitting the threshold of damage creation linked to the molten phase.[56] For Ti and Zr the extracted values are in agreement with the calculated ones using Eq. (5) if the number of electrons per atom of $z=2$ is assumed. However a four times lower g value was measured in fs laser experiments for Ti, pointing to $z=1$. This may be related to the high electronic excitation induced by the heavy ions as compared to the low excitation by laser. But what is more important is that the g values are deduced from the melt phase and used for particle evaporation from the vapor phase.

Another important parameter is the time during which the lattice stays above the vaporization temperature. This time depends on the lattice thermal conductivity K_l and on whether or not superheating occurs. If we assume superheating and a thermal conductivity calculated from the thermal diffusivity within the kinetic gas theory[52] an overall agreement was obtained with the measured yields. It is clear that increasing K_l without superheating would also reproduce the experimental data. But then we would have to insert an unrealistic value for K_l. Open questions concern the validity of the extrapolated values which are used for the specific heat and the thermal diffusivity at temperatures well above the evaporation temperature. Regarding all these uncertainties on the lattice parameters, the calculations in the present paper were performed in the same way as the previous ones[16,22,23] in order to be consistent.

The implementation of nuclear heating has introduced two new parameters. As said before the calculation is not very sensitive to the deposition time τ. A more sensitive parameter is R_0, the cylinder radius, in which most of the nuclear collision energy is deposited. We have used the mean range of lattice atoms with a mean energy as deduced from elastic scattering. However, nothing is known about the effective size of a nuclear spike at our high energies.

An additional energy transport mechanism could be the pressure pulse necessarily connected to the fast density change of the liquid or vapor phase. A rough estimate gives a value of 5 GPa which may also contribute to sputtering. Such a mechanism was proposed by Jakas *et al.*[57] to explain the large measured sputtering yields of rare gases and by Bringa and Johnson[58] to simulate an ionic spike. The observed overcosine angular distribution has also been seen in molecular dynamics (MD) calculations[59] and may be an indication of a pressure pulse contribution similar to the recently found jetlike component in LiF sputtering.[60]

V. CONCLUSION

Sputtering experiments with swift heavy ions on metals such as Ti and Zr have given clear evidence for electronic effects, i.e., an influence of the electronic energy loss S_e on the sputtering yield. Using appropriate ion/energy combinations an increase of the sputtering yield is seen with increasing S_e but with constant nuclear energy loss S_n. A similar effect is observed by varying the ion charge state which is known to affect S_e. Doubling the charge state under otherwise unchanged conditions increases the sputtering yield significantly. Both findings cannot be explained by a linear collision cascade theory, i.e., nuclear sputtering. In contrast to Ti and Zr no such electronic effects have been observed in sputtering of Au targets. This behavior was in accordance with the expectation of an inelastic thermal spike model which deposits the energy loss after an energetic heavy ion impact in matter primarily in the electronic subsystem and transfers it subsequently to the atoms by electron-phonon interaction.

The measured yields are not as large as, for example, in electronic sputtering of insulators, but definitely above the predictions of a collision cascade theory. The existing TS model was extended, therefore, to simulate electronic sputtering by an evaporation process of particles. However electronic heating alone was not sufficient to evaporate Zr atoms and the nuclear energy loss input of the ions had to be considered in addition. This extra heating mechanism was modeled using the well-known concept of an elastic collision (nuclear) spike. Simulations with electronic and nuclear heating together reproduced the measured yields of Zr and Ti within a factor of 2. Metal sputtering seems to be the first case in which a synergy of both heating mechanisms can be

clearly seen, apparently due to comparable contributions from electronic and nuclear effects—in contrast to insulators. The inclusion of a nuclear spike component in our TS model also explained the difference between the measured yield and the MC simulation for Au, even in the range of some hundred MeV.

The sputter calculations used the same set of parameters as has been successfully used for the simulation of track formation in metals and, hence, the new inelastic TS model has established a link between damage creation (melt phase) and sputtering (vapor phase). Further experiments are in preparation to measure the energy distribution of sputtered particles which could provide another signature for thermal contributions (electronic or nuclear) to sputtering at high energies.

ACKNOWLEDGMENTS

This work has been supported by the Deutsche Forschungsgemeinschaft (DFG) under Grant No. AS 102. We appreciate the initial help of H. Glückler and M. Brodale on this project, the generous support by Professor Stritzker's Institute at the University Augsburg with target preparation, RBS, XRD, and transmission electron microscopy analyses, and RBS analysis by R. Grötzschel at FZ Rossendorf. Finally, we thank Friedhelm Bell for many helpful discussions and Maria Assmann for a careful reading of the manuscript.

*Present address: Deutsches Patent- und Markenamt, D-80297 München, Germany.

†On leave from Institute of Modern Physics, Lanzhou 730000, China.

[1] J.E. Griffith, R.A. Weller, L.E. Seiberling, and T.A. Tombrello, Radiat. Eff. **51**, 223 (1980).

[2] R.E. Johnson and W.L. Brown, Nucl. Instrum. Methods Phys. Res. **198**, 103 (1982).

[3] P. Sigmund, Phys. Rev. **184**, 383 (1969).

[4] P.K. Haff, Appl. Phys. Lett. **29**, 473 (1976).

[5] T.A. Tombrello, Nucl. Instrum. Methods Phys. Res. B **2**, 555 (1984).

[6] F. Seitz and J.S. Koehler, Solid State Phys. **2**, 305 (1956).

[7] R.L. Fleischer, P.B. Price, and R.M. Walker, J. Appl. Phys. **36**, 3645 (1965).

[8] L.E. Seiberling, J.E. Griffith, and T.A. Tombrello, Radiat. Eff. **52**, 201 (1980).

[9] I.A. Baranov, Yu.V. Martynenko, S.O. Tsepelevich, and Yu.N. Yavlinski, Usp. Fiz. Nauk **156**, 477 (1988) [Sov. Phys. Usp. **31**, 1015 (1988)].

[10] K. Wien, Radiat. Eff. Defects Solids **109**, 137 (1989).

[11] J.P. O'Connor, L.M. Baumel, P.G. Blauner, K.M. Hubbard, M.R. Weller, and R.A. Weller, Nucl. Instrum. Methods Phys. Res. B **13**, 365 (1986).

[12] J.P. O'Connor, P.G. Blauner, and R.A. Weller, Nucl. Instrum. Methods Phys. Res. **218**, 293 (1983).

[13] S. Klaumünzer and G. Schumacher, Phys. Rev. Lett. **51**, 1987 (1983).

[14] S. Klaumünzer, M.D. Hou, and G. Schumacher, Phys. Rev. Lett. **57**, 850 (1986).

[15] A. Audouard *et al.*, Phys. Rev. Lett. **65**, 875 (1990).

[16] Ch. Dufour, A. Audourd, F. Beuneu, J. Dural, J.P. Girard, A. Hairie, M. Levalois, E. Paumier, and M. Toulemonde, J. Phys.: Condens. Matter **5**, 4573 (1993).

[17] A. Dunlop and D. Lesueur, Radiat. Eff. Defects Solids **126**, 123 (1993).

[18] A. Barbu, A. Dunlop, D. Lesueur, and R.S. Averback, Europhys. Lett. **15**, 37 (1991).

[19] H. Dammak, A. Dunlop, D. Lesueur, A. Brunelle, S. Della-Negra, and Y. Le Beyec, Phys. Rev. Lett. **74**, 1135 (1995).

[20] H.H. Andersen, A. Brunelle, S. Della-Negra, J. Depauw, D. Jacquet, Y. Le Beyec, J. Chaumont, and H. Bernas, Phys. Rev. Lett. **80**, 5433 (1998).

[21] S. Bouneau, A. Brunelle, S. Della-Negra, J. Depauw, D. Jacquet, Y. Le Beyec, M. Pautrat, M. Fallavier, J.C. Poizat, and H.H. Andersen, Phys. Rev. B **65**, 144106 (2002).

[22] Z.G. Wang, Ch. Dufour, E. Paumier, and M. Toulemonde, J. Phys.: Condens. Matter **6**, 6733 (1994).

[23] Ch. Dufour, F. Beuneu, E. Paumier, and M. Toulemonde, Europhys. Lett. **45**, 585 (1999).

[24] H.D. Mieskes, W. Assmann, M Brodale, M. Dobler, H. Glückler, P. Hartung, and P. Stenzel, Nucl. Instrum. Methods Phys. Res. B **146**, 162 (1998).

[25] W. Assmann, P. Hartung, H. Huber, P. Staat, H. Steffens, and Ch. Steinhausen, Nucl. Instrum. Methods Phys. Res. B **85**, 726 (1994).

[26] S. Hémon, Ch. Dufour, F. Gourbilleau, E. Paumier, E. Dooryhée, and S. Bégin-Colin, Nucl. Instrum. Methods Phys. Res. B **146**, 443 (1998).

[27] A. Gutzmann, S. Klaumünzer, and P. Meier, Phys. Rev. Lett. **74**, 2256 (1995).

[28] M. Küstner, W. Eckstein, V. Dose, and J. Roth, Nucl. Instrum. Methods Phys. Res. B **145**, 320 (1998).

[29] H.D. Mieskes, Ph.D. thesis, University of Munich, 1999.

[30] W.O. Hofer, in *Sputtering by Particle Bombardment III*, edited by R. Behrisch and K. Wittmaack (Springer, Berlin, 1991).

[31] S. Bouffard, J.P. Duraud, M. Mosbah, and S. Schlutig, Nucl. Instrum. Methods Phys. Res. B **141**, 372 (1998).

[32] J.P. Biersack, Nucl. Instrum. Methods Phys. Res. B **27**, 21 (1987); J. P. Biersack, computer code TRIM-CASCADE (HMI, Berlin, Germany, 1992).

[33] H.H. Andersen, A. Johansen, and V.S. Touboltsev, Nucl. Instrum. Methods Phys. Res. B **164-165**, 727 (2000).

[34] V.I. Shulga, Nucl. Instrum. Methods Phys. Res. B **164-165**, 733 (2000).

[35] J.F. Ziegler, J.P. Biersack, and U. Littmark, *The Stopping and Range of Ions in Solids* (Pergamon, New York, 1985); J.F. Ziegler, computer code SRIM96 (IBM, Yorktown, NY, 1996).

[36] L.E. Seiberling, C.K. Meins, B.H. Cooper, J.E. Griffith, M.H. Mendenhall, and T.A. Tombrello, Nucl. Instrum. Methods Phys. Res. **198**, 17 (1982).

[37] C.M. Frey, G. Dollinger, A. Bergmaier, T. Faestermann, and P. Maier-Komor, Nucl. Instrum. Methods Phys. Res. B **107**, 31 (1996).

[38] A. Blazevic, H.G. Bohlen, and W. von Oertzen, Nucl. Instrum. Methods Phys. Res. B **190**, 64 (2002).

[39] J.P. Biersack and W. Eckstein, Appl. Phys. A: Solids Surf. **A34**, 73 (1984).

[40] G. Schiwietz, G. Xiao, E. Luderer, and P.L. Grande, Nucl. Instrum. Methods Phys. Res. B **164-165**, 353 (2000).
[41] M.P.R. Waligorski, R.N. Hamm, and R. Katz, Nucl. Tracks Radiat. Meas. **11** (6), 309 (1986).
[42] H. Dammak, D. Lesueur, A. Dunlop, P. Legrand, and J. Morillo, Radiat. Eff. Defects Solids **126**, 111 (1993).
[43] A. Dunlop, D. Lesueur, P. Legrand, H. Dammak, and J. Dural, Nucl. Instrum. Methods Phys. Res. B **90**, 330 (1994).
[44] S.D. Brorson, A. Kazeroonian, J.S. Moodera, D.W. Face, T.K. Cheng, E.P. Ippen, M.S. Dresselhaus, and G. Dresselhaus, Phys. Rev. Lett. **64**, 2172 (1990).
[45] I.M. Kaganov, I.M. Lifshitz, and L.V. Tanatarov, Zh. Éksp. Teor. Fiz. **31**, 273 (1956) [Sov. Phys. JETP **4**, 173 (1957)].
[46] Ch. Dufour, F. Beuneu, E. Paumier, and M. Toulemonde, Europhys. Lett. **45**, 585 (1999).
[47] Ch. Dufour, Z.G. Wang, M. Levalois, P. Marie, E. Paumier, F. Pawlak, and M. Toulemonde, Nucl. Instrum. Methods Phys. Res. B **107**, 218 (1996).
[48] A. Meftah, F. Brisard, J.M. Costantini, M. Hage-Ali, J.P. Stoquert, F. Studer, and M. Toulemonde, Phys. Rev. B **48**, 920 (1993).
[49] Z.G. Wang, Ch. Dufour, B. Cabeau, J. Dural, G. Fuchs, E. Paumier, F. Pawlak, and M. Toulemonde, Nucl. Instrum. Methods Phys. Res. B **107**, 175 (1996).
[50] M. Toulemonde, Ch. Dufour, Z.G. Wang, and E. Paumier, Nucl. Instrum. Methods Phys. Res. B **112**, 26 (1996).
[51] P. Sigmund and C. Claussen, J. Appl. Phys. **52**, 990 (1981).
[52] P. Sigmund, Appl. Phys. Lett. **25**, 169 (1974); **27**, 52 (1975).
[53] S. Williamson, G. Mourou, and J.C.M. Li, Phys. Rev. Lett. **52**, 2364 (1984).
[54] P. Hermes, B. Danielzik, N. Fabricius, D. von der Linde, J. Luhl, Y. Heppner, B. Stritzker, and A. Pospieszcyk, Appl. Phys. A: Solids Surf. **39**, 9 (1986).
[55] Chr. Lehman, in *Interaction of Radiation with Solids*, edited by S. Amelinckx, R. Gevers, and J. Nihoul (North-Holland, Amsterdam, 1977).
[56] Ch. Dufour, Z.G. Wang, E. Paumier, and M. Toulemonde, Bull. Mater. Sci. **22**, 671 (1999).
[57] M.M. Jakas, E.M. Bringa, and R.E. Johnson, Phys. Rev. B **65**, 165425 (2002).
[58] E.M. Bringa and R.E. Johnson, Phys. Rev. Lett. **88**, 165501 (2002).
[59] H.M. Urbassek, Nucl. Instrum. Methods Phys. Res. B **122**, 427 (1997).
[60] M. Toulemonde, W. Assmann, C. Trautmann, and F. Grüner, Phys. Rev. Lett. **88**, 057602 (2002).